manuscript submitted to *Permafrost and Periglacial Processes*

Seesaw-like Elevational Dependence of Permafrost Temperature Warming and Active Layer Thickening on the Qinghai-Tibet Plateau

Hailong Ji[1], Shuping Zhao[2], Zhuotong Nan[2,3*]

[1] State Key Laboratory of Climate System Prediction and Risk Management, Nanjing Normal University, Nanjing, 210023, China

[2] Yangtze River Delta Urban Wetland Ecosystem National Field Scientific Observation and Research Station, School of Environmental and Geographical Sciences, Shanghai Normal University, Shanghai, 200234, China

[3] Jiangsu Center for Collaborative Innovation in Geographical Information Resource Development and Application, Nanjing, 210023, China

* Corresponding author: Zhuotong Nan(nanzt@shnu.edu.cn)

How to cite:

Ji H, Zhao S, Nan Z. Seesaw-Like Elevational Dependence of Permafrost Temperature Warming and Active Layer Thickening on the Qinghai–Tibet Plateau. Permafrost and Periglacial Processes. 2026. doi:https://doi.org/10.1002/ppp.70054.

Abstract

Elevation-dependent warming (EDW) is a well-documented feature of climate change in mountain regions, yet how it influences elevation-dependent permafrost change (EDPC) remains poorly understood. Here, we combine multi-forcing ensemble simulations, a novel block-sampling approach, and in-situ observations to investigate regional EDPC on the Qinghai-Tibet Plateau (QTP) over the past four decades. The simulations reveal a robust seesaw-like EDPC: in low-elevation warm permafrost (3800–4600 m), active layer thickness (ALT) thickens more rapidly (−0.06 to −0.24 m $10a^{-1}$ per 1000 m), whereas in high-elevation cold permafrost (4800–5600 m), temperature at the top of permafrost (TTOP) warms more rapidly (0.05–0.20 °C $10a^{-1}$ per 1000 m). This pattern is consistently supported by observations from 54 permafrost stations, which show a similar temperature-dependent seesaw relationship. We demonstrate that the seesaw-like EDPC is dominated by subsurface surplus heat partitioning, governed primarily by initial permafrost temperature through the soil freezing characteristic curve, rather than by external EDW or local environmental factors. The pattern remains stable across the full range of historical and most projected future EDW scenarios, indicating that it represents a fundamental mode of alpine permafrost degradation. These findings provide a new thermodynamic framework for understanding regional permafrost change and highlight the critical role of internal heat partitioning in shaping the response of high-mountain permafrost to climate warming.

Keywords

Permafrost change; Elevation-dependent warming; Elevation-dependent permafrost change, Qinghai-Tibet Plateau, Heat partitioning

1 Introduction

Permafrost underlies approximately 15% of the Northern Hemisphere land surface (Obu, 2021), with major occurrences in circum-Arctic regions and the Qinghai-Tibet Plateau (QTP). As a critical component of cold-region systems, permafrost regulates ecosystems, hydrological cycles, and infrastructure stability. Ongoing atmospheric warming is driving widespread permafrost degradation (Smith et al., 2022; Zhao et al., 2021), manifested primarily as rising temperature at

the top of permafrost (TTOP) and thickening of the active layer (ALT). These changes have profound implications for the terrestrial carbon budget (Bao et al., 2025; Mu et al., 2025), water resources (Xiang et al., 2016; Xu et al., 2024), runoff generation (Del Vecchio et al., 2024; Wang et al., 2023), and geomorphological processes (Li et al., 2021; Luo et al., 2019). Given its fundamental role, understanding regional patterns of permafrost baseline conditions and their temporal evolution remains a high priority in permafrost science.

The QTP is the world's largest alpine permafrost region. Since the 1980s, Cheng (1984) established the zonation of alpine permafrost, primarily governed by elevation, latitude, and aridity, with the lower permafrost limit showing a strong elevational dependence attributed to the atmospheric lapse rate (~6.5 °C per 1000 m). This permafrost elevation model has been repeatedly validated and forms a cornerstone of our understanding of alpine permafrost distribution (Cheng & Francesco, 1992; Harris et al., 2017; Riseborough et al., 2008). Nevertheless, consensus on regional-scale patterns of permafrost change has yet to emerge due to the complexity itself and the limitation in current methodology.

Permafrost functions as a thermodynamic system whose long-term evolution is governed by climate-induced anomalies in surface heat input, termed "surplus heat". Under the simplifying assumption of spatially uniform surplus heat input, the response of permafrost, a system involving ice-water transition, is determined by how this surplus heat is partitioned between sensible (raising ground temperature) and latent heat (melting ground ice). This partitioning is well described by the soil freezing characteristic curve (SFCC), which relates unfrozen water content to subzero temperature (Kurylyk & Watanabe, 2013; Painter & Karra, 2014; Romanovsky et al., 2010). Near the freezing point, a greater fraction of surplus heat is consumed as latent heat, favoring ALT thickening; farther below the freezing point, more heat contributes to sensible warming, favoring TTOP rise. Consequently, warm permafrost tends to exhibit higher sensitivity in ALT, while cold permafrost shows higher sensitivity in TTOP. Given the pronounced elevational gradient in permafrost temperatures across the QTP (Cheng, 1984; Cheng & Francesco, 1992), this mechanism implies a potential "seesaw-like" elevation-dependent permafrost change (EDPC): faster ALT thickening at lower elevations (warm permafrost) and faster TTOP warming at higher elevations (cold permafrost), with the two trends crossing along the elevation gradient.

In reality, however, surplus heat is rarely uniform. Numerous studies document elevation-dependent air warming (EDW) in mountain regions worldwide, including the QTP, typically

characterized by amplified warming rates at higher elevations (i.e., positive EDW) (Byrne et al., 2024; Pepin et al., 2015; You et al., 2020). Positive EDW would introduce heterogeneous surplus heat inputs, potentially reinforcing the positive elevation gradient in TTOP change rates while compensating for the lower ALT sensitivity of cold permafrost, thereby weakening or even eliminating the negative elevation gradient in ALT change rates. Under strong EDW (positive or negative), both TTOP and ALT change rates could exhibit unidirectional elevational trends, precluding a seesaw-like EDPC. Additionally, local factors such as snow cover, vegetation, soil texture, and moisture influence heat and water transfer (Clayton et al., 2021; Fu et al., 2025), potentially modulating or overriding the regional signal of EDPC. Specifically, these local factors have nontrivial impacts on the shape of SFCC (Painter & Karra, 2014; Stuurop et al., 2021) and thus the surplus heat partitioning. Therefore, the existence or non-existence of a regional seesaw-like EDPC depends on the outcome of competition among external surplus heat input (modulated by EDW), subsurface heat transfer (related to local factors), and internal heat partitioning (manifested as SFCC).

However, investigating EDPC at the plateau scale is challenging for three reasons. First, in-situ observations of both EDW and EDPC are sparse and unevenly distributed due to logistical constraints, limiting their representativeness for regional conditions (Miao et al., 2024). Second, model simulations, while offering spatially comprehensive insights, are sensitive to uncertainties in meteorological forcing datasets, which often exhibit cold and wet biases over the rugged QTP terrain (Lun et al., 2021; You et al., 2015). Different forcing products can yield conflicting EDW signals (positive, negative, or absent), with unclear propagation into simulated permafrost changes (Guo et al., 2021; You et al., 2020). Third, the QTP spans broad elevational (3000–7000 m), longitudinal (75–105 °E), and latitudinal (25–40 °N) gradients; variations in surface energy balance and subsurface properties along longitude and latitude can confound pure elevational signals (Wang et al., 2016).

To address these challenges and resolve the existence and controls of regional EDPC, we (1) performed multi-forcing ensemble simulations using a modified Noah Land Surface Model (Noah-Tibet) to generate robust historical permafrost changes; (2) applied a block-sampling method to isolate elevational signals from longitudinal and latitudinal interference; (3) developed a hypothesis-testing framework to identify the dominant controls on surplus heat partitioning; and (4) conducted targeted EDW scenario experiments to obtain the marginal conditions under which

the seesaw-like EDPC persists. These efforts reveal a robust historical seesaw-like EDPC on the QTP, advance mechanistic understanding of its controls, and clarify its sensitivity to EDW.

2 Materials and Methods

2.1 Study area

The QTP, located in Central Asia (75–105 °E and 25–40 °N), covers an area of 2.45×10^6 km^2 with a mean elevation exceeding 4000 m (Figure 1a). Major mountain ranges, including the Himalayas, Karakoram, and Gangdise, create strong elevational gradients. Mean annual air temperature (MAAT) ranges from −8.2 °C to 4.9 °C (10th–90th percentile), and decreases markedly with elevation. Permafrost typically occurs where MAAT is below −2 °C, corresponding to elevations above approximately 3500–4000 m (Cheng & Francesco, 1992). Under present climate conditions, permafrost underlies about 1.08×10^6 km^2 of the QTP (Cao et al., 2023; Zou et al., 2017). The observed ALT generally ranges from 1.8 to 4.6 m regionally (see Figure S2 for distribution), with a mean annual ground temperature (MAGT) of approximately −1.6 °C (Wu et al., 2015; Zhao et al., 2021). In contrast to the circum-Arctic permafrost region, the QTP features thin snow cover and sparse vegetation (Che et al., 2015; Hou & Zhang, 2021). In the cold season (October–February), mean snow depth rarely exceeds 3 cm (Figure 1b1), and alpine grassland and barren land dominate the land cover (Figure 1b2).

2.2 Dataset and preprocessing

The in-situ monitoring network comprises weather and permafrost stations. Observations from weather stations were obtained from the Station-Based Serially Complete Earth (SC-Earth) Dataset (Tang et al., 2021). These stations are primarily located in seasonally frozen ground at low elevations, with only 69 stations publicly available (Figure 1a). For permafrost observations, we used the dataset compiled by Fu et al. (2025), which integrates records from Wu et al. (2015), Zhang et al. (2020) and Zhao et al. (2021). This dataset provides ALT and TTOP for 54 long-term stations along the Qinghai-Tibet Highway during 2001-2020. These in-situ data were used to evaluate the representativeness of regional climate and permafrost conditions and to validate Noah-Tibet. Additionally, air temperature change rates (1980–2018) from 416 meteorological stations across the QTP (69 stations) and its adjacent regions (70–110° E, 20–45° N, 347 stations) were extracted from the SC-Earth dataset to compare with gridded EDW signals.

Given the large uncertainties in meteorological data over the QTP, four forcing datasets were employed to drive Noah-Tibet: the China Meteorological Forcing Dataset from the Institute of Tibetan Plateau Research (ITP-Forcing, 0.1 °, 1979–2018, 3-hourly) (He et al., 2020), the Third Pole High-Resolution Precipitation Dataset (TPHiPr, 1/30 °, 1979–2020, Hourly) (Jiang et al., 2023), the enhanced land component of the fifth European Centre for the Medium-Range Weather Forecasts reanalysis (ERA5-Land, 0.1°, 1950-present, hourly) (Muñoz-Sabater et al., 2021), and the MODIS-based bias-corrected reanalysis downscaled dataset for daily mean air temperature (MBRD, 1 km, 1980–2014, daily) (Zhang et al., 2021). These datasets generally agree with station observations (Hu et al., 2019; Yuan et al., 2021), although discrepancies remain in data sparse high-elevation areas. The ITP-Forcing was selected as the baseline forcing dataset because it provides all required meteorological variables and is widely used in QTP studies (Wang et al., 2023; Wu et al., 2018). Four forcing datasets for the Noah-Tibet were constructed by replacing air temperature and/or precipitation components in ITP-Forcing with those from the other datasets (see Table S2 for details). All datasets were aggregated or truncated to align with the spatiotemporal resolution and coverage of ITP-Forcing. For MBRD, the diurnal cycle of air temperature was reconstructed using the pattern from ITP-Forcing while preserving the daily mean from MBRD. In addition, a high-resolution Coupled Model Intercomparison Project 6 downscaled daily Climate Projections over China dataset (Yuan et al., 2024) was used to determine the possible EDW range on the QTP, serving the design of EDW scenario simulation. Details of these and auxiliary datasets (e.g., snow depth, soil texture, elevation) are provided in Table S1.

2.3 Numerical simulation

2.3.1 Historical simulation

In our previous work (Chen et al., 2015; Wu et al., 2018), the Noah LSM (Ek et al., 2003) was modified to better represent permafrost processes on the QTP, resulting in the Noah-Tibet model. Key modifications included improved parameterizations of surface roughness length, soil thermal and hydraulic conductivities, and extension of the soil column to 15.2 m depth with 18 layers. A 500-year spin-up is required for a realistic simulation of multi-decadal permafrost change (Ji et al., 2022). Details of the model modifications and validation against in-situ observations are provided in Text S1, Text S2 and Figure S1.

Four ensemble experiments (EXP1–4) were conducted for the historical period (1980s–2010s) to account for forcing uncertainty (Table S2). EXP1 used the full ITP-Forcing. EXP2 replaced

precipitation in ITP-Forcing with TPHiPr to address potential overestimation of wetting trends. EXP3 and EXP4 were based on EXP2 but replaced air temperature with ERA5-Land and MBRD, respectively.

2.3.2 EDW scenario simulation

To explore the competition between EDW and surplus heat partitioning in shaping EDPC, we designed a suite of idealized 40-year warming scenario experiments using Noah-Tibet. Building on the conceptual framework presented in the Introduction, strong EDW could disrupt the seesaw-like pattern by altering the elevational gradients of the change rate of TTOP ($TTOP_{CR}$) and the change rate of ALT (ALT_{CR}). Specifically, positive EDW may compensate for the lower climate sensitivity of ALT_{CR} in cold permafrost at high elevations, while negative EDW may compensate for the lower climate sensitivity of $TTOP_{CR}$ of warm permafrost at low elevations.

Eleven EDW scenarios were constructed, ranging from −0.25 to 0.25 °C $10a^{-1}$ per 1000m at intervals of 0.05 °C $10a^{-1}$ per 1000m, informed by climate model projections (Table S3). It should be noted that climate projection data were introduced solely to define plausible EDW scenarios, rather than to predict future EDPC, which would require more computationally intensive transient simulations. Within each scenario, ten elevation bands (200 m intervals from 3800 m to 5600 m) were defined. Baseline climate for each window was derived from the early 1980s conditions (to avoid potential bias associated with anomalous conditions in a single year) within ±100 m of the target elevation band. Warming rates were applied such that the domain-wide average warming rate remained 0.4 °C $10a^{-1}$ (referencing the regional average warming rate) while satisfying the prescribed EDW gradient. A total of 110 simulations (11 EDW scenarios × 10 elevation bands) were performed. Details of the experimental design are given in Text S3.

The seesaw-like EDPC was considered disrupted when the elevational gradient of ALT_{CR} (for positive EDW) or $TTOP_{CR}$ (for negative EDW) lost statistical significance at the 95% confidence level based on linear regression. This approach quantifies the marginal EDW conditions under which surplus heat partitioning no longer dominates the pattern. Note that atmospheric warming remains the primary driver of permafrost degradation; the scenario experiments only examine the relative influence of EDW versus heat partitioning in shaping the mode of permafrost change.

2.3.3 Model output processing

Daily profiles of soil temperature, moisture, and unfrozen water content were output for all 18 layers. Permafrost was identified in each grid cell when at least one soil layer remained frozen (≤ 30 °C) for both the current and previous year (van Everdingen, 1998). ALT was defined as the maximum seasonal thaw depth, with TTOP taken as the mean annual soil temperature at that depth.

2.4 Quantifying surplus heat partitioning

Surplus heat partitioning between sensible and latent heat near the base of the active layer was diagnosed from simulated soil temperature and moisture fields using the energy balance formulation (Equations 1–3). Sensible heat consumption ($|H_S|$) for a given soil layer is calculated as:

$$|H_S| = \sum_{k_1}^{k_2} \frac{C_{soil}(k) \cdot |\Delta ST(k)| \cdot Z(k)}{86400} \qquad (1)$$

$$C_{soil}(k) = \sum_i \theta_i(k) \cdot C_i(k) \qquad (2)$$

where C_{soil} is the volumetric heat capacity of the soil (J m^{-3} °C^{-1}), ΔST is the daily change in soil temperature (°C), and Z is the layer thickness (m). C_{soil} is calculated as the volumetrically weighted average of soil constituents (Equation 2): C_{liq}=4.2×10^6 J m^{-3} °C^{-1}, C_{ice}=2.1×10^6 J m^{-3} °C^{-1}, C_{solid}=2.0×10^6 J m^{-3} °C^{-1}, C_{air}=1004 J m^{-3} °C^{-1}. θ_i (m^3 m^{-3}) was extracted from model outputs. Latent heat consumption ($|H_L|$) is given by:

$$|H_L| = \sum_{k_1}^{k_2} \frac{L \cdot \rho_{liq} \cdot |\Delta ICE(k)| \cdot Z(k)}{86400} \qquad (3)$$

where L is the latent heat of fusion (3.34×10^5 J kg^{-1}), ρ_{liq} is the density of liquid water (1000 kg m^{-3}), and ΔICE is the daily change in ice content (m^3 m^{-3}).

To avoid cancellation effects arising from daily warming/cooling and freezing/thawing cycles, absolute values of H_S and H_L were used. Without taking the absolute values, summing the daily sensible and latent heat would merely approximate the difference between the first and last day, thus losing substantial information on surplus heat consumption and resulting in highly unstable outcomes. Finally, the ratio of sensible heat consumption, $|H_S|/(|H_S| + |H_L|)$, was then calculated to quantify the partitioning of surplus heat. Given the regional distribution of ALT (typically 1–4 m; Figure S2), layers 8–10 of the model (k_1 and k_2, corresponding to depths of 1.5–4.2 m) were selected to represent conditions near the base of the active layer across most of the QTP permafrost

region. This depth range ensures robust coverage of the active layer bottom under varying local ALT conditions.

2.5 Statistical methodology

Elevation bands from 3800 to 5600 m were defined using 200 m intervals (±100 m), yielding 10 bins (3800±100 m, 4000±100 m, …, 5600±100 m) that encompass the majority of permafrost regions on the QTP (Figure 1b3). For each variable (e.g., MAAT change rate or $MAAT_{CR}$, $TTOP_{CR}$, ALT_{CR}), grid-cell trends were first calculated via linear regression, after which the median value within each bin was used to represent that elevation band. Elevational gradients were then quantified by regressing these bin medians against elevation.

To minimize confounding effects from longitude and latitude on detected elevational signals, a block-sampling method was applied (Figure S3). For each of the four historical simulations, 500 permafrost grid cells were randomly selected as centers to construct 2×2° (about 400 km^2) windows (~400 grid cells per window). Only windows containing more than 25% permafrost cells were retained to ensure adequate representativeness. Within each valid window, anomalies were computed by subtracting the window mean from each grid-cell value. These anomalies were then aggregated by elevation band. The median across all valid windows was used to characterize the regional EDPC signal. This anomaly-based procedure effectively isolates the elevational gradient from biases associated with areal weighting. When analyzing the evolution of the elevation dependence of permafrost states over the past four decades, the elevation zoning across the entire study was utilized to present the elevational gradient of raw values rather than anomaly values, as well as facilitating comparison with future studies.

3 Results

3.1 Revisiting in-situ observations

Only 69 weather stations and 54 permafrost stations are available across the vast QTP (2.45×10^6 km^2) and its permafrost region (1.08×10^6 km^2) (Figure 1a). Their limited and uneven distribution severely constrains their representativeness for regional climate and permafrost conditions. Joint analysis of elevation-MAAT (Figure 1c1, c3) and longitude-MAAT (Figure 1c2, c4) distributions further reveals this limitation. Most weather stations are located at lower elevations in seasonally frozen ground, with very few above 4600 m or west of 90 °E, where permafrost is most extensive. The 54 permafrost stations are heavily clustered between 4600–5200 m and near 93 °E, far from

the continuous permafrost zones (Figure 1a). Although additional local weather stations exist, they are generally less accessible and predominantly situated at low elevations, offering limited improvement in regional representativeness. In recent decades, new permafrost monitoring networks have been established through field campaigns, particularly in data-scarce regions (Zhao et al., 2021). However, their relatively short record lengths preclude robust long-term trend analysis. Consequently, existing in-situ observations cannot adequately capture the spatial patterns of climate and permafrost changes (e.g., EDW and EDPC) across the entire plateau.

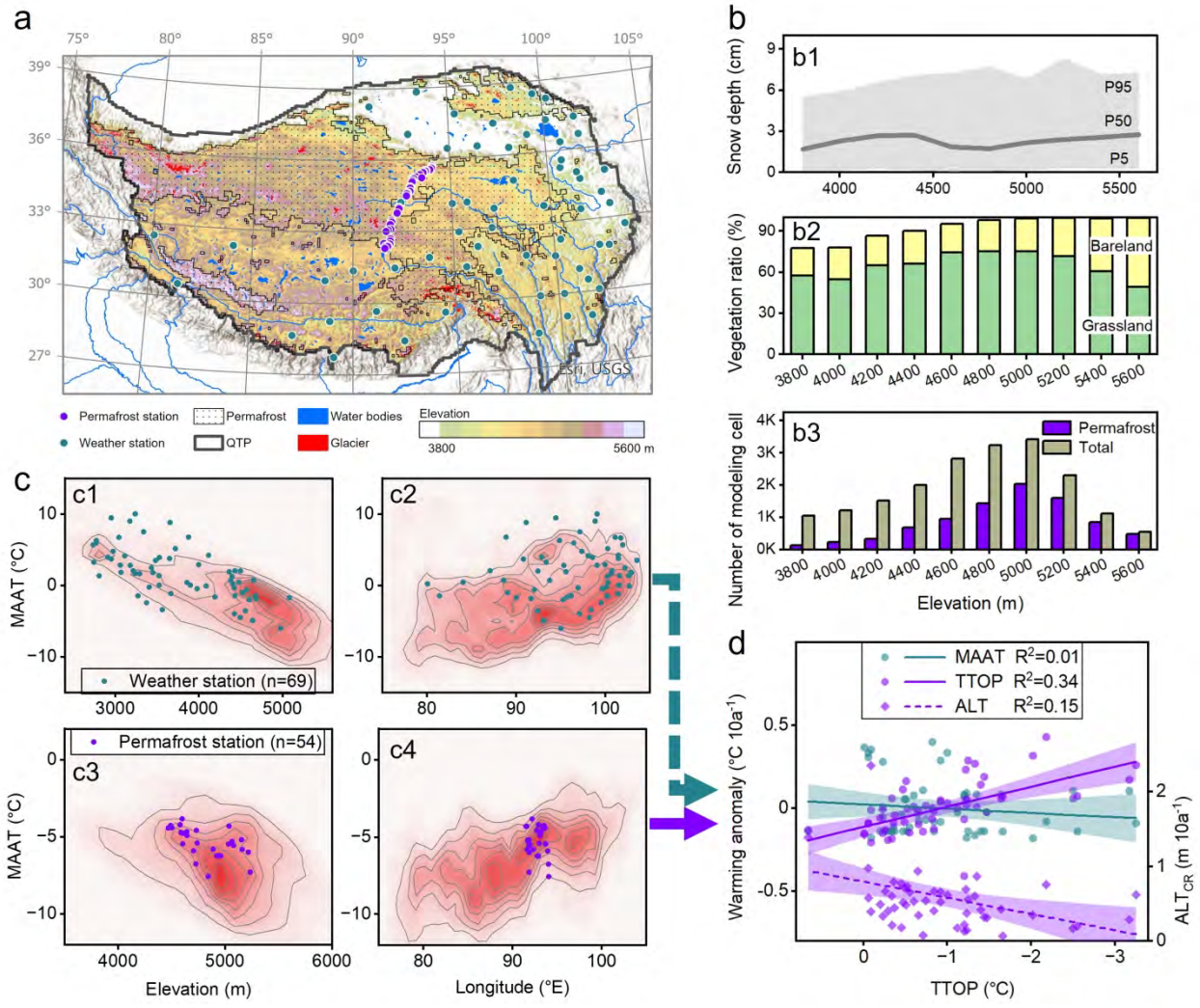

Figure 1 Overview of the study area, in-situ observation network, and their representativeness. (a) Spatial distribution of permafrost (based on Noah-Tibet ensemble simulations), weather stations (teal dots, n=69), permafrost stations (purple dots, n=54), and elevation across the Qinghai-Tibet Plateau (QTP). (b) Environmental characteristics of QTP: (b1) variations in cold-season (October–February) mean snow depth, (b2) dominant land cover types (grassland and bareland), and (b3) the number of permafrost/land cells along elevation within the permafrost region. P5, P50, and P95 denote the 5th, 50th, and 95th percentiles of snow depth during the cold season. (c) Joint distributions of elevation versus mean annual air temperature (MAAT) and longitude

versus MAAT, showing the limited representativeness of the in-situ stations. Red shading indicates the density of grid cells across the entire QTP or permafrost region (darker colors for higher density). MAAT was derived from the ITP-Forcing climatology (1979–2018). (d) Relationships between the change rates of MAAT, temperature at the top of permafrost (TTOP), and active layer thickness (ALT) versus decadal mean TTOP at the 54 permafrost stations (2001–2020). MAAT change rates were averaged from three gridded datasets (ITP-Forcing, ERA5-Land, and MBRD).

Despite these limitations, the in-situ records still offer valuable insight into permafrost responses to climate change. At the 54 permafrost stations during 2001–2020, $TTOP_{CR}$ and ALT_{CR} did not exhibit a clear seesaw-like elevational dependence, largely because the elevational range across these sites is only ~ 600 m and local heterogeneity (aspect, geomorphic unit, soil text, and vegetation) is strong. However, both change rates exhibited a distinct seesaw-like relationship with decadal mean TTOP: ALT_{CR} was larger in warm permafrost (higher mean TTOP), whereas $TTOP_{CR}$ was larger in cold permafrost (lower mean TTOP). Notably, $MAAT_{CR}$ showed only weak correlation with mean TTOP, suggesting limited differences in surplus heat input among the sites. The pattern suggests that surplus heat partitioning outweighed the influence of atmospheric forcing and local environmental factors at the site scale. A similar seesaw-like relationship between permafrost change rates and mean ground temperature has also been observed across northern hemisphere permafrost regions (Smith et al., 2022).

Although the site-level seesaw pattern occurs along the temperature gradient rather than elevation per se, it suggests that a regional-scale seesaw-like EDPC may exist on the QTP, given the strong elevational dependence of permafrost temperature (Cheng, 1984) (Figure 1c3). Model simulations are therefore essential to test whether this pattern holds at the plateau scale after accounting for EDW and other confounding factors.

3.2 Simulated historical EDPC

The Noah-Tibet model accurately reproduces the spatial pattern and temporal evolution of permafrost conditions on the QTP, including the observed seesaw-like relationship between $TTOP_{CR}$, ALT_{CR}, and mean TTOP (Text S1, Text S2 and Figure S1). This provides confidence in using the ensemble simulations to examine the regional scale EDPC.

To minimize confounding effects from longitude and latitude, the block sampling was applied to both the meteorological forcing datasets and the simulation outputs (Figure S3). Analysis of the meteorological forcing datasets revealed a weak negative EDW signal across the QTP permafrost region (−0.01–−0.04 °C $10a^{-1}$ per 1000 m; Figure 2a); that is, air warming depresses at higher elevations. This pattern contrasts with the positive EDW commonly reported from low-elevation

weather stations (You et al., 2020), but agrees with some recent studies at higher elevations on the QTP (Guo et al., 2019; Zhang et al., 2022) as well as in-situ observations (as detailed in Section 4.1).

Under the weak negative EDW, the multi-forcing ensemble simulations (EXP1–4) produced a clear seesaw-like EDPC (Figure 2b, c): $TTOP_{CR}$ was faster at high elevations (0.05–0.20 °C $10a^{-1}$ per 1000 m), whereas ALT_{CR} was faster at low elevations (−0.06–−0.24 m $10a^{-1}$ per 1000 m). These results indicate that surplus heat partitioning between sensible and latent components surpassed the influence of EDW as well as environmental factors in controlling the trajectory of regional permafrost degradation over recent decades.

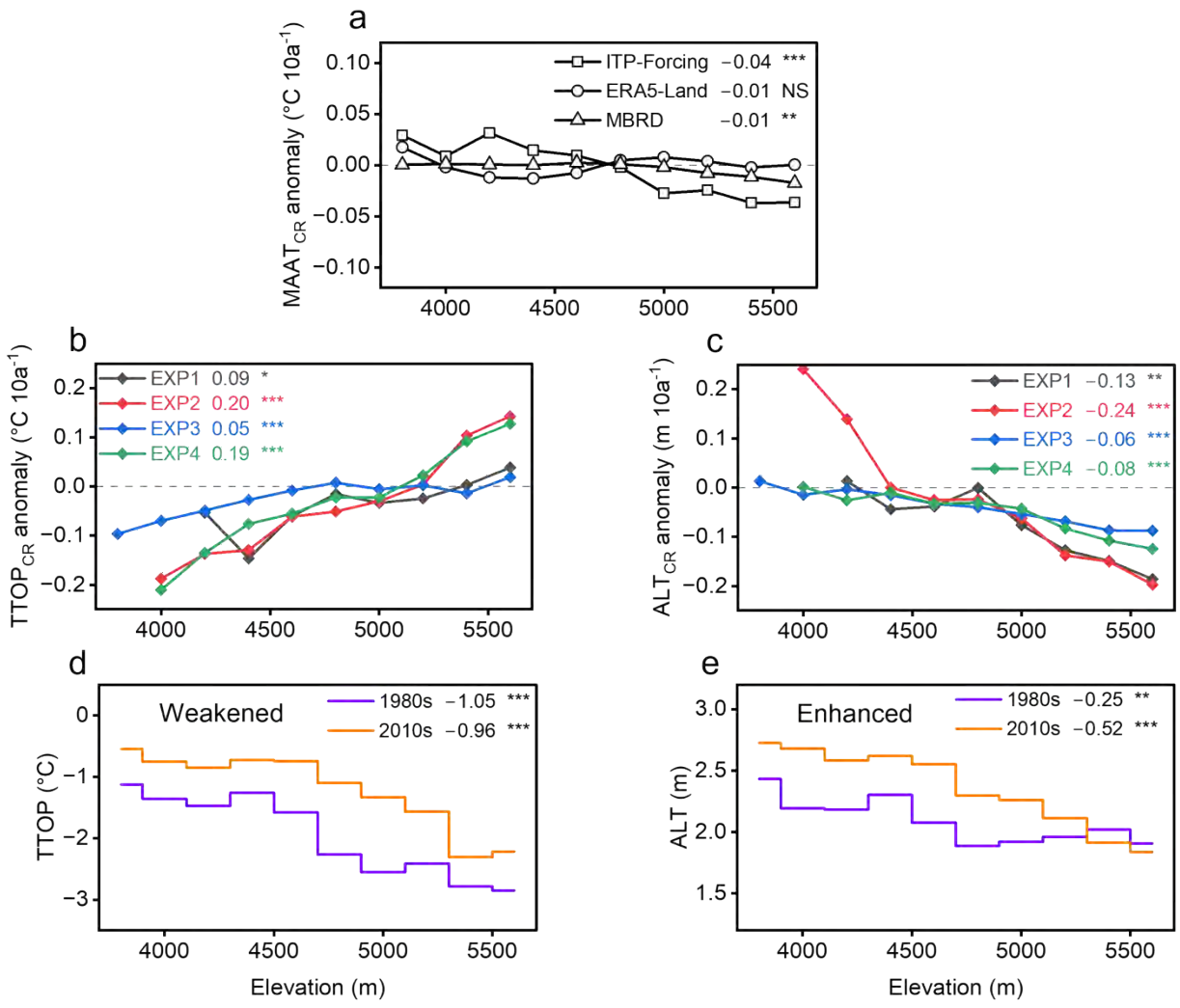

Figure 2 Simulated elevation-dependent permafrost change (EDPC). (a) Elevational dependence of the change rate of mean annual air temperature ($MAAT_{CR}$) derived from the three meteorological forcing datasets (ITP-Forcing, ERA5-Land, MBRD). (b, c) Elevational dependence of the change rate of TTOP ($TTOP_{CR}$) and ALT (ALT_{CR}) from the multi-forcing ensemble simulations

*(EXP1–4). (d, e) Elevational dependence of decadal mean TTOP and ALT. In (a–e), the elevational gradients (per 1000 m) are labeled, with significance levels marked as *** ($p<0.001$), ** ($p<0.01$), * ($p<0.05$), NS ($p\geq0.05$). In (d, e), ensemble means are shown for simplicity, and direct elevational binning was applied to present actual values, whereas block sampling was used in (a–c) to minimize longitudinal and latitudinal interference.*

Over the past four decades, the seesaw-like EDPC has weakened the elevational dependence of TTOP (from −1.05 °C per 1000 m in the 1980s to −0.96 °C per 1000 m in the 2010s; Figure 2d) but enhanced that of ALT (from −0.25 m per 1000 m in the 1980s to −0.52 m per 1000 m in the 2010s; Figure 2e). In the low-elevation (3800–4600 m) warm permafrost regions, TTOP increased by 1.01 °C, ALT thickened by 0.22 m, whereas in high-elevation (4800–5600 m) cold permafrost, TTOP increased by 0.67 °C and ALT thickened by 0.38 m. Conceptual diagrams illustrating the contrasting responses of warm permafrost at lower elevations (latent heat-dominated ALT thickening) and cold permafrost at higher elevations (sensible heat-dominated TTOP warming) are shown in Figure 3.

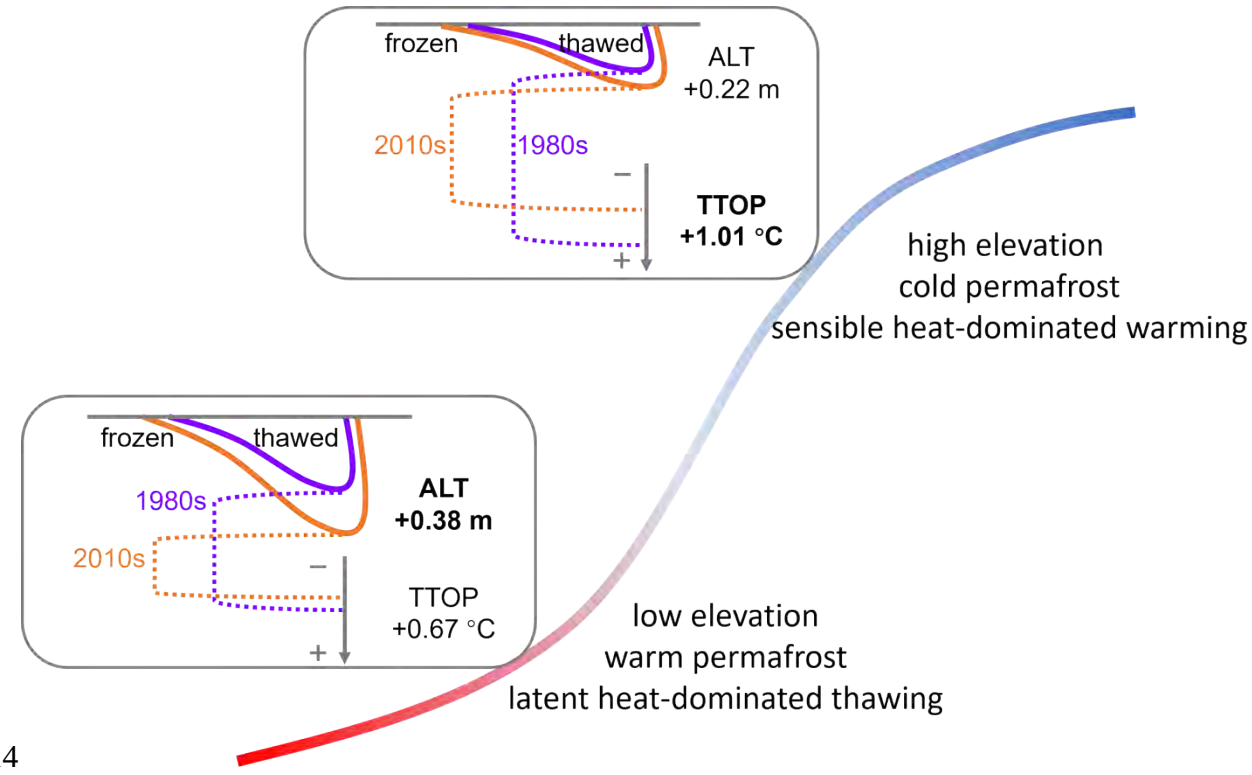

Figure 3 Conceptual diagram of the seesaw-like EDPC. The gradient shading from red to blue represents the transition from low to high elevation and the corresponding decrease in permafrost temperature. The two inserts illustrate the contrasting permafrost responses in low-elevation (3800–4600 m) warm permafrost and high-elevation (4800–5600 m) cold permafrost. Solid curves depict the movement of the thawing front, where the deepest depth corresponds to the ALT and mean soil temperature at that depth is TTOP. The straight lines with arrows and plus/minus signs indicate the direction and relative magnitude of temperature change (positive for warming). Note that the downward orientation of these arrows is intended for layout clarity and does not represent

physical depth. The schematic is intended for conceptual illustration and does not imply that the seesaw-like EDPC occurs at the slope scale, as it was derived from regional simulations.

3.3 Underlying mechanism

Both station observations (Figure 1d) and regional simulations (Figure 2b,c) demonstrate that the partitioning of surplus heat governs the "seesaw-like" permafrost change, validating our theoretical deduction. However, this does not imply that permafrost temperature (e.g., mean TTOP) is the sole determinant, as non-thermal factors can also influence surplus heat partitioning by modulating the morphology of the SFCC. To identify the dominant controls on surplus heat partitioning, a hypothesis-testing framework was established based on SFCC (Kurylyk & Watanabe, 2013; Romanovsky et al., 2010) and regional environments. Three candidate factors were examined: ground ice content near the base of the active layer, soil porosity (as a proxy for soil texture), and TTOP (Figure 4a-c). With increasing elevation, the simulated ground ice content increases, corresponding to lower TTOP and smaller soil porosity (i.e., coarser soil texture). The simulated relationship between ground ice and elevation aligns with recent ground ice mapping studies (Wang et al., 2026; Zou et al., 2024), both suggesting that thermal conditions remain the primary determinant of ground ice content on the QTP.

These factors lead to three corresponding hypotheses (Figure 4d). Hypothesis 1 is predicated on the principle that ground ice content determines the upper limit of latent heat consumption, corresponding to the increment along the vertical axis of the SFCC (Figure 4d). For an identical ALT increment, lower elevations with lower ice content require less total heat for melting. Under relatively uniform surplus heat input, ALT at lower elevations would change more rapidly, thereby favoring a negative elevation gradient for ALT_{CR}. Hypothesis 2 posits that soil texture influences water retention capacity and heat capacity, corresponding to the maximum unfrozen water content in the SFCC (Figure 4d). Soils at lower elevations exhibit higher porosity and lower coarse-grained content, leading to better water retention and wetter soil conditions generally. Within the wetter active layer, a considerable portion of heat is consumed as latent heat during seasonal freeze-thaw cycles, leaving only a small fraction to alter soil temperature and propagate into the deeper layer. This seasonal-scale surplus heat partitioning is expected to persist under climate change. Furthermore, the specific heat capacity of water is significantly higher than that of soil particles or air, facilitating slower soil warming. Consequently, this favors a positive elevation gradient for $TTOP_{CR}$. Hypothesis 3 is based on the premise that temperature determines the operating position on the SFCC; the closer the temperature is to the freezing point, the steeper the curve, meaning an

identical temperature change corresponds to a greater change in unfrozen water content (i.e., ice melt) (Figure 4d). As elevation increases and mean TTOP decreases, a larger proportion of surplus heat is utilized to change soil temperature, leading to faster TTOP changes (a positive elevation dependence). Correspondingly, the elevation dependence of ALT change is negative.

The ratio of sensible heat consumption (relative to the total surplus heat consumption) at the active layer bottom can effectively test these three hypotheses. As elevation increases, the ratio increases (Figure 4e), which contradicts Hypothesis 1 but supports Hypotheses 2 and 3. If Hypothesis 1 were valid, then the latent heat effect would be weak in low elevations with the low ice content, resulting in a higher ratio of sensible heat consumption. In contrast, Hypotheses 2 and 3 predict that an active layer with either fine soil texture (high porosity) or near-freezing temperature should exhibit a lower ratio of sensible heat consumption. To further distinguish between Hypotheses 2 and 3, a partial correlation analysis was conducted among the sensible heat consumption ratio, TTOP, and soil porosity. The results (Figure 4f) reveal that the partial correlation coefficient with TTOP ranges from −0.88 to −0.79, while the absolute value of the correlation with soil porosity does not exceed 0.11. Although TTOP may influence soil texture or porosity through altering the frequency and magnitude of freeze-thaw cycles, given the weak correlation between the two at the regional scale, these partial correlation results strongly support Hypothesis 3. In summary, initial permafrost temperature, through its regulation of the intensity of ice-water phase change along the SFCC, is the primary factor governing surplus heat partitioning and thereby shaping the seesaw-like EDPC on the QTP.

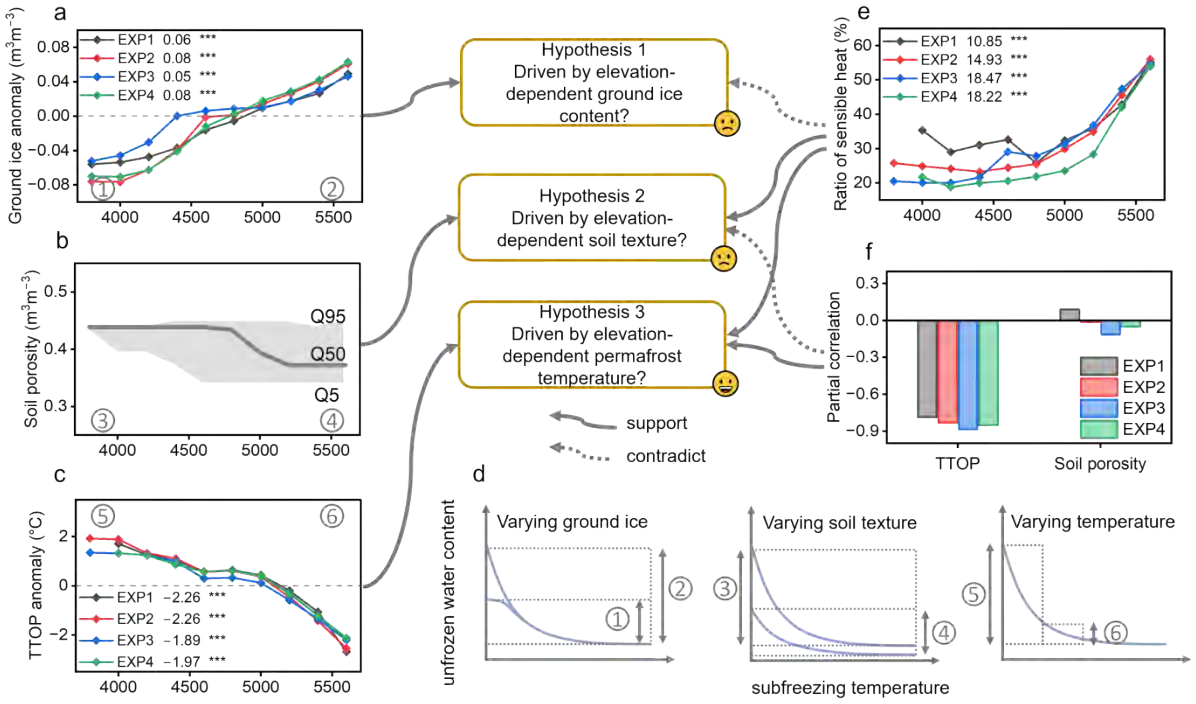

*Figure 4 Hypothesis-testing framework for identifying the dominant factor controlling surplus heat partitioning. (a–c) Elevational dependence of the three candidate factors: ground ice content, soil porosity, and TTOP. (d) Schematic diagrams illustrating how these factors affect surplus heat partitioning through the soil freezing characteristic curve. (e) Elevational dependence of the ratio of sensible heat consumption to total surplus heat consumption. (f) Partial correlation analysis among the ratio of sensible heat consumption, TTOP, and soil porosity. In (a–d), circled numbers are shared: odd numbers correspond to low-elevation warm permafrost (low ice content, fine soil texture, and relatively high subfreezing temperature), and even numbers are for high-elevation cold permafrost (high ice content, coarse soil texture, and low subfreezing temperature). In (a, c, e), elevational gradients (per 1000 m) are labeled, with statistical significance marked as *** ($p<0.001$), ** ($p<0.01$), * ($p<0.05$), NS ($p\geq0.05$). Results from the four ensemble experiments (EXP1–4) are used.*

4 Discussion

4.1 Anomalous negative EDW at high elevations

A central and unexpected finding of this study is the persistence of a weak negative EDW signal across the QTP permafrost regions (−0.01 to −0.04 °C $10a^{-1}$ per 1000 m; Figure 2a). This contrasts sharply with the positive EDW commonly observed at low elevations and reported across mid-latitude mountain ranges (Byrne et al., 2024; Pepin et al., 2015; You et al., 2020). Station-based observation reinforces that the negative signal is a genuine regional feature rather than an artifact of gridded forcing products (Figure 5). The observations across 416 weather stations exhibit that EDW is positive in the 0–4800 m range (gradient of 0.04 °C $10a^{-1}$ per 1000m; Figure 5b), aligning with current consensus (Byrne et al., 2024). However, within the key permafrost one (3800–4800

1m), observations across 27 weather stations show a subtle negative EDW (−0.01 °C $10a^{-1}$ per 1000
2m; Figure 5b), which closely matches the gridded datasets in the overlapping elevation range
3(Figure 5c).

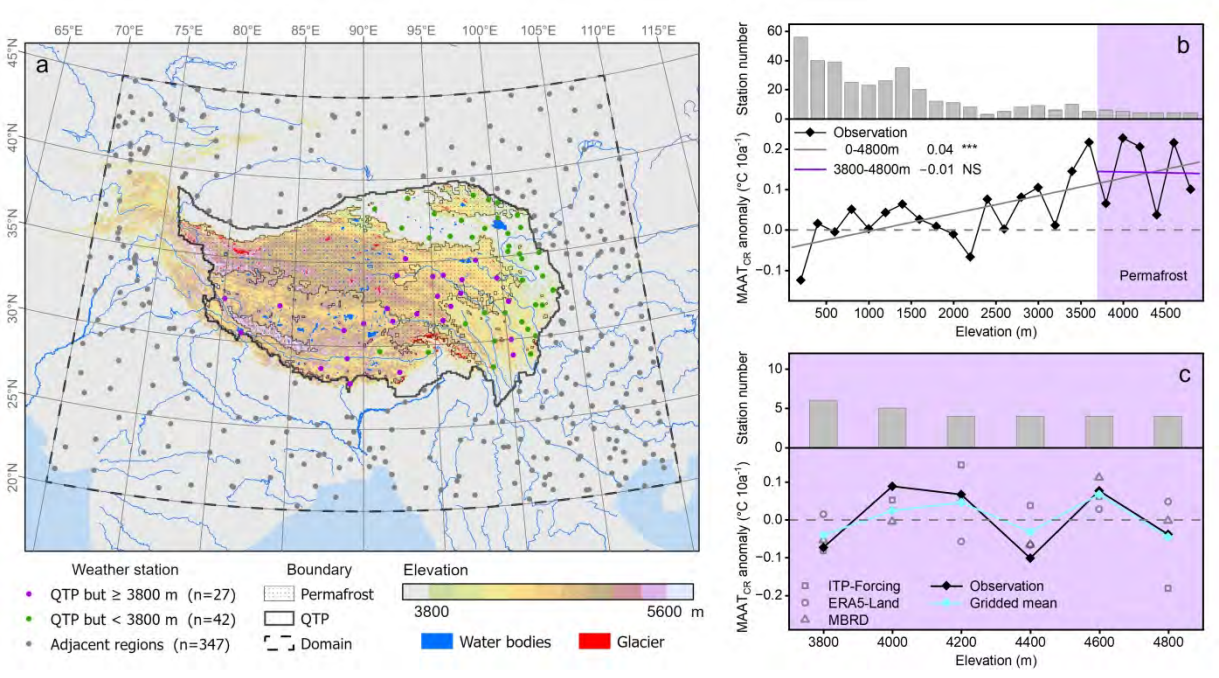

4

5*Figure 5 Elevation-dependent air warming (EDW) on the QTP and its adjacent regions (70-110 °E, 20-45 °N). (a) Spatial*
6*distribution of the 416 weather stations used in the analysis, including 69 stations located on the QTP, with data derived from SC-*
7*Earth dataset (Tang et al., 2021). (b) Elevation variation in the change rate of MAAT ($MAAT_{CR}$) and the number of stations. (c)*
8*Same as (b) but zoomed in on the permafrost domain (above 3800 m). In (b), elevational gradients (per 1000 m) are labeled, with*
9*statistical significance indicated as *** (p<0.001), ** (p<0.01), * (p<0.05), NS (p≥0.05). To facilitate comparison, $MAAT_{CR}$*
10*anomalies were calculated by removing the regional mean (0-4800 m for panel (b) and 3800-4800 m for (c)).*

11We interpret this anomalous EDW as a consequence of the exceptionally high baseline elevations
12(mostly above 3800 m) of the QTP permafrost region. At such elevations, the snow-albedo
13feedback, which typically drives positive EDW at mid-to-high elevations by reducing snow cover
14and lowering surface albedo with warming (Rangwala et al., 2016), may be less effective or even
15reversed due to increased winter precipitation leading to greater snow accumulation and higher
16albedo (Guo et al., 2021; Zhang et al., 2022). Additionally, enhanced cloud cover, changes in
17atmospheric water vapor, or local topographic and circulation effects specific to the plateau's high
18interior cloud introduce cooling influences or dampen warming (Abbas et al., 2024; Hua et al.,
192018). Other mechanisms, such as increased evapotranspiration or aerosol effects (Rangwala et
20al., 2010), might also play a role but are likely secondary. Although these mechanisms require
21targeted process studies, the finding demonstrates that EDW is not a universal feature of mountain

regions but is highly sensitive to elevation range and geographic context. This has important implications for understanding climate feedbacks in the highest alpine permafrost zones and challenges the direct extrapolation of mid-elevation EDW relationships to extremely high-elevation environments.

4.2 Robustness of the seesaw-like EDPC

We designed a suite of idealized 40-year warming scenario experiments to identify the critical EDW thresholds at which the elevation dependence of either $TTOP_{CR}$ or ALT_{CR} reverses, essentially defining the conditions under which the seesaw-like EDPC ceases to exist. The experiments reveal that the seesaw-like EDPC is remarkably robust (Table 1). The pattern persists across a wide range of EDW intensities (−0.15 to +0.10 °C $10a^{-1}$ per 1000 m), encompassing both historical conditions (−0.04 to −0.01 °C $10a^{-1}$ per 1000m) and most CMIP6-projected future scenarios for the QTP. Only under strongly negative or strongly positive EDW do the elevational gradients of $TTOP_{CR}$ or ALT_{CR} lose statistical significance.

Specifically, for $TTOP_{CR}$, the surplus heat partitioning mechanism inherently favors a positive elevation dependence. The scenario simulations demonstrate that a negative elevation dependence for $TTOP_{CR}$ only emerges when the EDW is less than or equal to −0.20 °C $10a^{-1}$ per 1000m. Moreover, its positive elevation dependence loses statistical significance ($p > 0.05$) when the EDW reaches −0.15 °C $10a^{-1}$ per 1000m, which we define as the critical EDW for reversing the $TTOP_{CR}$ trend. Conversely, for ALT_{CR}, where surplus heat partitioning typically drives a negative elevation dependence, the critical EDW that renders this trend non-significant at the 95% confidence level is 0.10 °C $10a^{-1}$ per 1000m. Although these scenario experiments are not intended as specific projections under future climate change, based on projected EDW ranges (Table S3), it can be inferred that the seesaw-like EDPC is likely to persist.

This result carries significant implications. It indicates that the seesaw-like EDPC is not a transient phenomenon but a fundamental mode of alpine permafrost response under climate change. As the QTP continues to warm at more than 1.5 times the global average rate, the persistence of this pattern will have profound implications for regional hydrology, carbon cycling, and the resilience of high-altitude ecosystems and infrastructure, issues that warrant urgent attention in both scientific research and climate adaptation planning.

Table 1 Simulated elevation gradients of the change rate of TTOP ($TTOP_{CR}$) and ALT (ALT_{CR}) under idealized EDW scenarios. Bold p-values indicate non-significant trends ($p \geq 0.05$).

EDW (°C $10a^{-1}$ per 1000m)	Elevation-dependent $TTOP_{CR}$ (°C $10a^{-1}$ per 1000m)	p-value	Elevation-dependent ALT_{CR} (m $10a^{-1}$ per 1000m)	p-value
−0.25	−0.04	**0.602**	−0.08	0.009
−0.20	−0.01	**0.754**	−0.07	0.016
−0.15	0.08	**0.210**	−0.06	0.016
−0.10	0.10	0.007	−0.05	0.016
−0.05	0.12	< 0.001	−0.05	0.016
0.00	0.18	< 0.001	−0.05	0.029
0.05	0.20	< 0.001	−0.03	0.048
0.10	0.23	< 0.001	−0.01	**0.602**
0.15	0.26	< 0.001	0.02	**0.348**
0.20	0.29	< 0.001	0.03	**0.175**
0.25	0.32	< 0.001	0.03	**0.118**

4.3 Strengths and limitations

This study makes two broader contributions to permafrost science. Methodologically, the integration of multi-forcing ensembles with a novel block-sampling technique provides a transferable framework for isolating elevational signals in complex mountain terrain, an approach applicable to other high-mountain permafrost regions. Conceptually, we introduce a unified thermodynamic framework that treats permafrost degradation as the outcome of competition among surplus heat input (modulated by EDW), transfer (influenced by local factors), and partitioning (governed by the SFCC). This framework explains why heat partitioning, regulated primarily by initial permafrost temperature, emerges as the dominant control on the form of degradation (latent heat-dominated thawing at lower elevations versus sensible heat-dominated warming at higher elevations). By demonstrating that this partitioning-driven seesaw pattern holds across observational and modeling scales, the study advances beyond descriptive accounts toward a process-based understanding that can inform both regional assessments and global modeling efforts.

Despite this, the limitations of the Noah-Tibet model must be acknowledged. Same with most land surface and permafrost models (e.g., CLM, CoLM, Noah-MP, and SHAW), the Noah-Tibet permits only pore ice rather than excess ice. The primary challenge in integrating excess ice lies in the fact that the fixed-layer soil schemes used in classical process-based models are no longer

applicable. Several modeling efforts have attempted to address this. For instance, CryoGrid 3 Xice (Westermann et al., 2016) employs a one-dimensional redistribution scheme that swaps meltwater and overlying solid material, leading to subsidence or thermokarst ponding depending on lateral drainage conditions. Sun et al. (2022) developed a moving-mesh permafrost model that treats soil and ice layers as a deformable elastomer. However, due to the lack of regional-scale information on excess ice distribution, these integrated models are not yet feasible for large-scale simulations. Consequently, the omission of excess ice may reduce the reliability of simulated changes in ice-rich permafrost regions.

On the QTP, excess ice is dominated by segregated ice (Lin et al., 2020), which is primarily concentrated near the permafrost table as pure or sediment-rich ice layers ranging from several centimeters to several meters in thickness. Compared to soil layers containing only pore ice, the presence of segregated ice significantly enhances thermal conductivity (Ji et al., 2024), leading to more pronounced seasonal variations in soil temperature. Over longer timescales, the substantial latent heat effects of segregated ice allow it to act as a thermal buffer. Surplus heat must first melt the pure ice layers before the ALT can deepen (whereas the reference baseline only requires melting ice-bearing soil). As a result, models that neglect segregated ice tend to systematically overestimate both ALT_{CR} and $TTOP_{CR}$. This is supported by scenario simulations; for instance, Lee et al. (2014) demonstrated that excess ice could reduce the projected increase in soil temperature at a 1 m depth by 0.35 °C during the 1860–2100 period. Regarding ALT, if measured from the ground surface, the associated subsidence partially compensates for the increase in ALT (O'Neill et al., 2023). Therefore, the latent heat-related response of permafrost to climate change encompasses both the increase in ALT and the magnitude of subsidence.

While the absence of segregated ice may introduce systematic biases in model simulation, ground ice content across the study area is relatively limited. According to a recently published distribution map of volumetric ice content (VIC) within the top 5 m of Northern Hemisphere permafrost (Wang et al., 2026), the VIC of permafrost in China (dominated by the QTP) mostly ranges between 20% and 40%, with a mean of 32.25%, only about half of the values typical in circum-Arctic regions. Ground ice mapping by Zou et al. (2024) specifically for the QTP shows VIC values of 28.4%, 30.2%, and 29.2% at depths of 2–3 m, 3–5 m, and 5–10 m, respectively. Compared with the circum-Arctic, this regional discrepancy stems primarily from the relatively warm and arid climate, coarse soil textures, and low organic matter content of the QTP, which result in thermodynamic and hydraulic conditions less conducive to ground ice formation.

Note that both Wang et al. (2026) and Zou et al. (2024) provide estimates of total volumetric ice content (including both pore ice and segregated/excess ice) and do not distinguish between the two components. Therefore, these datasets offer only an indirect indication of segregated ice abundance on the QTP. Based on the current understanding of ground ice occurrence, fine-grained soils, poorly drained lowlands, or relatively flat terrains are more favorable for ice enrichment under suitable thermal conditions (Lin et al., 2020; Wang et al., 2026; Zou et al., 2024). At the hillslope scale, variations in these environmental factors may lead to significant spatial anomaly in ice content; however, at the regional scale, where elevation differences are primarily driven by tectonics, such local heterogeneity is unlikely to exert a systematic influence on large-scale patterns, that is, the seesaw-like EDPC.

In addition, the 0.1 ° resolution and one-dimensional structure of Noah-Tibet inherently cannot resolve local-scale topographic and ecological heterogeneity (Clayton et al., 2021; Smith et al., 2022) or lateral heat and water transfer. Given that most reanalysis products remain limited to 0.25° or coarser (Hu et al., 2019; Muñoz-Sabater et al., 2021; You et al., 2015), a 0.1° resolution represents the practical limit for multi-forcing ensemble simulations, achieved in this study by integrating disparate high-resolution datasets. Observations from a permafrost island on the QTP show that lateral thawing rates driven by horizontal thermal gradients can be nearly five times higher than vertical thawing rates (Jin et al., 2006). Similarly, Hamm and Frampton (2021) demonstrated using the Advanced Terrestrial Simulator that subsurface runoff can create pronounced differences in permafrost temperature and ALT between downhill and uphill positions over distances of less than 100 m. Although approaches such as lateral tile coupling (Aas et al., 2019) have been proposed to adapt one-dimensional models to small-scale permafrost processes, these methods are not yet implemented in Noah-Tibet.

Nevertheless, because this study focuses on regional-scale patterns, these resolution limitations are unlikely to affect the robustness of the seesaw-like EDPC identified across the QTP. We emphasized that the regional seesaw-like EDPC should not be directly extrapolated to the hillslope scale (Figure 3). Future work should quantify the spatial scale at which the seesaw-like EDPC transitions or diminishes. This would not only deepen our understanding of the competition between surplus heat input, transfer and partitioning, but also help reconcile discrepancies between in-situ observations and model simulations. Establishing intensified observation networks would greatly advance permafrost scaling research (Schneider von Deimling et al., 2021), similar to progress made in the field of soil moisture. More broadly, the extent to which the seesaw-like

EDPC on the QTP shapes regional hydrological cycles, ecological processes, carbon budgets, and thermokarst hazards warrants further investigation. For instance, Ji et al. (2026) showed that vegetation expansion in this region follows a pattern of both upward and downward migration. Exploring the coupling between permafrost changes and vegetation expansion/greening along elevation gradients remains a compelling scientific frontier.

4 Conclusions

This study provides the first robust demonstration of a seesaw-like elevation-dependent permafrost change (EDPC) across the QTP. By integrating multi-forcing ensemble simulations, a novel block-sampling approach, in-situ observations, and targeted EDW scenarios experiments, we reveal that permafrost degradation on the QTP follows a clear elevational pattern: TTOP warms more rapidly at higher elevations, while ALT thickens more rapidly at lower elevations. This pattern is primarily controlled by internal surplus heat partitioning governed by initial permafrost temperature through the soil freezing characteristic curve, rather than by external elevation-dependent atmospheric warming (EDW) or local environmental factors. The key conclusions are as follows:

(1) Over the past four decades, the QTP has exhibited a robust seesaw-like EDPC. Quantitatively, TTOP warmed by 0.67 °C and ALT thickened by 0.38 m in low-elevation (3800–4600 m) warm permafrost, compared with 1.01 °C and 0.22 m in high-elevation (4800–5600 m) cold permafrost. This pattern is consistently supported by both regional simulations and site-level observations showing a similar temperature-dependent seesaw relationship.

(2) The historical seesaw-like EDPC is dominated by subsurface surplus heat partitioning, which outweighs the influences of surface energy budget changes associated with EDW and environmental factors. Heat partitioning is primarily regulated by initial permafrost temperature, far exceeding the effects of ground ice content and soil texture. A new thermodynamic framework treating permafrost degradation as competition among surplus heat input, transfer, and partitioning successfully explains the observed elevational divergence in degradation modes.

(3) The seesaw-like EDPC is robust. It persists across a wide range of EDW intensities (−0.15 to +0.10 °C 10 a^{-1} per 1000 m), encompassing both historical conditions and most CMIP6-projected future scenarios. Only under extreme EDW does the pattern break down, indicating that the seesaw-like EDPC is likely to remain the dominant mode of alpine permafrost degradation on the QTP in the coming decades.

Conflict of Interest

The authors declare no conflicts of interest

Acknowledgments

This work is supported by National Natural Science Foundation of China (42571149).

Author Contributions

HJ: Conceptualization, Methodology, Validation, Formal analysis, Writing – Original Draft, Writing – Review & Editing; SZ: Resources, Writing – Original Draft, Writing – Review & Editing; ZN: Conceptualization, Investigation, Resources, Funding acquisition, Writing – Original Draft, Writing – Review & Editing, Supervision

Open Research

The study utilized the following publicly available datasets: Permafrost observations - (https://doi.org/10.6084/m9.figshare.29206613.v1), Observations of weather stations (https://zenodo.org/record/4762586), ITP-Forcing (https://doi.org/10.11888/AtmosphericPhysics.tpe.249369.file), TPHiPr (https://doi.org/10.11888/Atmos.tpdc.272763), ERA5-Land (https://doi.org/10.24381/cds.e2161bac), MBRD (https://doi.org/10.11888/Meteoro.tpdc.270377).

References

Aas, K. S., Martin, L., Nitzbon, J., et al. (2019). Thaw processes in ice-rich permafrost landscapes represented with laterally coupled tiles in a land surface model. *The Cryosphere*, *13*(2), 591-609. https://doi.org/10.5194/tc-13-591-2019

Abbas, H., Daramola, M. T., & Xu, M. (2024). Elevation-dependent warming and possible-driving mechanisms over global highlands. *International Journal of Climatology*, *44*(12), 4157-4177. https://doi.org/10.1002/joc.8572

Amatulli, G., Domisch, S., Tuanmu, M.-N., et al. (2018). A suite of global, cross-scale topographic variables for environmental and biodiversity modeling. *Scientific Data*, *5*(1), 180040. https://doi.org/10.1038/sdata.2018.40

Bao, T., Xu, X., Jia, G., et al. (2025). Climate-carbon feedback tradeoff between Arctic and alpine permafrost under warming. *Science Advances*, *11*(38), eadt8366. https://doi.org/10.1126/sciadv.adt8366

Byrne, M. P., Boos, W. R., & Hu, S. (2024). Elevation-dependent warming: observations, models, and energetic mechanisms. *Weather and Climate Dynamics*, *5*(2), 763-777. https://doi.org/10.5194/wcd-5-763-2024

Cao, Z., Nan, Z., Hu, J., et al. (2023). A new 2010 permafrost distribution map over the Qinghai-Tibet Plateau based on subregion survey maps: a benchmark for regional permafrost modeling. *Earth System Science Data*, *15*(9), 3905-3930. https://doi.org/10.5194/essd-2022-206

Che, T., Dai, L., & Li, X. (2015). *Long-term series of daily snow depth dataset in China (1979-2024)* National Tibetan Plateau Data Center. https://doi.org/10.11888/Geogra.tpdc.270194

Chen, H., Nan, Z., Zhao, L., et al. (2015). Noah modelling of the permafrost distribution and characteristics in the West Kunlun area, Qinghai-Tibet Plateau, China. *Permafrost and Periglacial Processes*, *26*(2), 160-174. https://doi.org/10.1002/ppp.1841

Cheng, G. (1984). Problems on zonation of high-altitude permafrost. *Acta Geographica Sinica*, *39*(2), 185-193. (in Chinese)

Cheng, G., & Francesco, D. (1992). Distribution of mountain permafrost and climate. *Permafrost and Periglacial Processes*, *3*(2), 83-91. https://doi.org/10.1002/ppp.3430030205

Clayton, L. K., Schaefer, K., Battaglia, M. J., et al. (2021). Active layer thickness as a function of soil water content. *Environmental Research Letters*, *16*(5), 055028. https://doi.org/10.1088/1748-9326/abfa4c

Del Vecchio, J., Palucis, M. C., & Meyer, C. R. (2024). Permafrost extent sets drainage density in the Arctic. *Proceedings of the National Academy of Sciences*, *121*(6), e2307072120. https://doi.org/10.1073/pnas.2307072120

Ek, M. B., Mitchell, K. E., Lin, Y., et al. (2003). Implementation of Noah land surface model advances in the National Centers for Environmental Prediction operational mesoscale Eta model. *Journal of Geophysical Research: Atmospheres*, *108*(D22), 8851. https://doi.org/10.1029/2002jd003296

Fu, Z., Wu, Q., Chen, A., et al. (2025). Non-temperature environmental drivers modulate warming-induced 21st-century permafrost degradation on the Tibetan Plateau. *Nature Communications*, *16*(1), 7556. https://doi.org/10.1038/s41467-025-63032-x

Guo, D., Pepin, N., Yang, K., et al. (2021). Local changes in snow depth dominate the evolving pattern of elevation-dependent warming on the Tibetan Plateau. *Science Bulletin*, *66*(11), 1146-1150. https://doi.org/10.1016/j.scib.2021.02.013

Guo, D., Sun, J., Yang, K., et al. (2019). Revisiting recent elevation-dependent warming on the Tibetan Plateau using satellite-based data sets. *Journal of Geophysical Research: Atmospheres*, *124*(15), 8511-8521. https://dx.doi.org/10.1029/2019jd030666

Hamm, A., & Frampton, A. (2021). Impact of lateral groundwater flow on hydrothermal conditions of the active layer in a high-Arctic hillslope setting. *The Cryosphere*, *15*(10), 4853-4871. https://doi.org/10.5194/tc-15-4853-2021

Harris, S. A., Brouchkov, A., & Guodong, C. (2017). *Geocryology: Characteristics and Use of Frozen Ground and Permafrost Landforms* (1st ed.). CRC Press. https://doi.org/10.4324/9781315166988

He, J., Yang, K., Tang, W., et al. (2020). The first high-resolution meteorological forcing dataset for land process studies over China. *Scientific Data*, *7*, 25. https://doi.org/10.1038/s41597-020-0369-y

Hou, X., & Zhang, X. (2021). *Vegetation Map of the People's Republic of China (1:1,000,000)* Plant Data Center of Chinese Academy of Sciences. https://doi.org/10.12282/plantdata.0155

Hu, G., Zhao, L., Wu, X., et al. (2019). Evaluation of reanalysis air temperature products in permafrost regions on the Qinghai-Tibetan Plateau. *Theoretical and Applied Climatology*, *138*(3), 1457-1470. https://doi.org/10.1007/s00704-019-02888-8

Hua, S., Liu, Y., Jia, R., et al. (2018). Role of clouds in accelerating cold-season warming during 2000–2015 over the Tibetan Plateau. *International Journal of Climatology*, *38*(13), 4950-4966. https://doi.org/10.1002/joc.5709

Ji, H., Fu, X., Nan, Z., et al. (2024). An effective medium theory-based unified model for estimating thermal conductivity of unfrozen and frozen soils. *CATENA*, *239*, 107942. https://doi.org/10.1016/j.catena.2024.107942

Ji, H., Nan, Z., Chen, Y., et al. (2026). Upslope and downslope vegetation expansions on the warming and wetting Qinghai–Tibet Plateau. *Environmental Research Letters*, *21*(4), 044022. https://doi.org/10.1088/1748-9326/ae436d

Ji, H., Nan, Z., Hu, J., et al. (2022). On the spin-up strategy for spatial modeling of permafrost dynamics: A case study on the Qinghai-Tibet Plateau. *Journal of Advances in Modeling Earth Systems*, *14*(3), e2021MS002750. https://doi.org/10.1029/2021MS002750

Jiang, Y., Yang, K., Qi, Y., et al. (2023). TPHiPr: a long-term (1979–2020) high-accuracy precipitation dataset (1⁄30°, daily) for the Third Pole region based on high-resolution atmospheric modeling and dense observations. *Earth System Science Data*, *15*(2), 621-638. https://doi.org/10.5194/essd-15-621-2023

Jin, H., Zhao, L., Wang, S., et al. (2006). Thermal regimes and degradation modes of permafrost along the Qinghai-Tibet Highway. *Science in China Series D-Earth Sciences*, *49*(11), 1170-1183. https://doi.org/10.1007/s11430-006-2003-z

Kurylyk, B. L., & Watanabe, K. (2013). The mathematical representation of freezing and thawing processes in variably-saturated, non-deformable soils. *Advances in Water Resources*, *60*, 160-177. https://doi.org/10.1016/j.advwatres.2013.07.016

Lee, H., Swenson, S. C., Slater, A. G., et al. (2014). Effects of excess ground ice on projections of permafrost in a warming climate. *Environmental Research Letters*, *9*, 124006. https://doi.org/10.1088/1748-9326/9/12/124006

Li, D., Lu, X., Overeem, I., et al. (2021). Exceptional increases in fluvial sediment fluxes in a warmer and wetter High Mountain Asia. *Science*, *374*(6567), 599-603. https://doi.org/10.1126/science.abi9649

Lin, Z., Gao, Z., Fan, X., et al. (2020). Factors controlling near surface ground-ice characteristics in a region of warm permafrost, Beiluhe Basin, Qinghai-Tibet Plateau. *Geoderma*, *376*, 114540. https://doi.org/10.1016/j.geoderma.2020.114540

Lun, Y., Liu, L., Cheng, L., et al. (2021). Assessment of GCMs simulation performance for precipitation and temperature from CMIP5 to CMIP6 over the Tibetan Plateau. *International Journal of Climatology*, *41*(7), 3994-4018. https://doi.org/10.1002/joc.7055

Luo, J., Niu, F., Lin, Z., et al. (2019). Recent acceleration of thaw slumping in permafrost terrain of Qinghai-Tibet Plateau: An example from the Beiluhe Region. *Geomorphology*, *341*, 79-85. https://doi.org/10.1016/j.geomorph.2019.05.020

Miao, C., Immerzeel, W. W., Xu, B., et al. (2024). Understanding the Asian water tower requires a redesigned precipitation observation strategy. *Proceedings of the National Academy of Sciences*, *121*(23), e2403557121. https://doi.org/10.1073/pnas.2403557121

Mu, C., Lei, P., Mu, M., et al. (2025). Methane emissions from thermokarst lakes must emphasize the ice-melting impact on the Tibetan Plateau. *Nature Communications*, *16*(1), 2404. https://doi.org/10.1038/s41467-025-57745-2

Muñoz-Sabater, J., Dutra, E., Agustí-Panareda, A., et al. (2021). ERA5-Land: a state-of-the-art global reanalysis dataset for land applications. *Earth System Science Data*, *13*(9), 4349-4383. https://doi.org/10.5194/essd-13-4349-2021

O'Neill, H. B., Smith, S. L., Burn, C. R., et al. (2023). Widespread Permafrost Degradation and Thaw Subsidence in Northwest Canada. *Journal of Geophysical Research: Earth Surface*, *128*(8), e2023JF007262. https://doi.org/10.1029/2023JF007262

Obu, J. (2021). How Much of the Earth's Surface is Underlain by Permafrost? *Journal of Geophysical Research: Earth Surface*, *126*(5), e2021JF006123. https://doi.org/10.1029/2021JF006123

Painter, S. L., & Karra, S. (2014). Constitutive Model for Unfrozen Water Content in Subfreezing Unsaturated Soils. *Vadose Zone Journal*, *13*(4), vzj2013.2004.0071. https://doi.org/10.2136/vzj2013.04.0071

Pepin, N., Bradley, R. S., Diaz, H. F., et al. (2015). Elevation-dependent warming in mountain regions of the world. *Nature Climate Change*, *5*, 424-430. https://doi.org/10.1038/nclimate2563

Rangwala, I., Miller, J. R., Russell, G. L., et al. (2010). Using a global climate model to evaluate the influences of water vapor, snow cover and atmospheric aerosol on warming in the Tibetan Plateau during the twenty-first century. *Climate Dynamics*, *34*(6), 859-872. https://doi.org/10.1007/s00382-009-0564-1

Rangwala, I., Sinsky, E., & Miller, J. R. (2016). Variability in projected elevation dependent warming in boreal midlatitude winter in CMIP5 climate models and its potential drivers. *Climate Dynamics*, *46*(7), 2115-2122. https://doi.org/10.1007/s00382-015-2692-0

Riseborough, D., Shiklomanov, N., Etzelmuller, B., et al. (2008). Recent advances in permafrost modelling. *Permafrost and Periglacial Processes*, *19*(2), 137-156. https://doi.org/10.1002/ppp.615

Romanovsky, V. E., Smith, S. L., & Christiansen, H. H. (2010). Permafrost thermal state in the polar Northern Hemisphere during the international polar year 2007-2009: a synthesis. *Permafrost and Periglacial Processes*, *21*(2), 106-116. https://dx.doi.org/10.1002/ppp.689

Schneider von Deimling, T., Lee, H., Ingeman-Nielsen, T., et al. (2021). Consequences of permafrost degradation for Arctic infrastructure – bridging the model gap between regional and engineering scales. *The Cryosphere*, *15*(5), 2451-2471. https://doi.org/10.5194/tc-15-2451-2021

Smith, S. L., O'Neill, H. B., Isaksen, K., et al. (2022). The changing thermal state of permafrost. *Nature Reviews Earth & Environment*, *3*(1), 10-23. https://doi.org/10.1038/s43017-021-00240-1

Stuurop, J. C., van der Zee, S. E. A. T. M., Voss, C. I., et al. (2021). Simulating water and heat transport with freezing and cryosuction in unsaturated soil: Comparing an empirical, semi-empirical and physically-based approach. *Advances in Water Resources*, *149*, 103846. https://doi.org/10.1016/j.advwatres.2021.103846

Sun, Z., Zhao, L., Hu, G., et al. (2022). Numerical simulation of thaw settlement and permafrost changes at three sites along the Qinghai-Tibet Engineering Corridor in a warming Climate. *Geophysical Research Letters*, *49*(10), e2021GL097334. https://doi.org/10.1029/2021GL097334

Tang, G., Clark, M. P., & Papalexiou, S. M. (2021). SC-Earth: A Station-Based Serially Complete Earth Dataset from 1950 to 2019. *Journal of Climate*, *34*(16), 6493-6511. https://doi.org/10.1175/JCLI-D-21-0067.1

van Everdingen, R. O. (1998). *Multi-language glossary of permafrost and related ground-ice terms*. http://globalcryospherewatch.org/reference/glossary_docs/Glossary_of_Permafrost_and_Ground-Ice_IPA_2005.pdf

Wang, B., Ran, Y., Li, X., et al. (2026). Near-surface ground ice map of the Northern Hemisphere. *Science Bulletin*, *71*(7), 1786-1797. https://doi.org/10.1016/j.scib.2026.02.028

Wang, Q., Fan, X., & Wang, M. (2016). Evidence of high-elevation amplification versus Arctic amplification. *Scientific Reports*, *6*(1), 19219. https://doi.org/10.1038/srep19219

Wang, T., Yang, D., Yang, Y., et al. (2023). Pervasive permafrost thaw exacerbates future risk of water shortage across the Tibetan Plateau. *Earth's Future*, e2022EF003463. https://doi.org/10.1029/2022EF003463

Westermann, S., Langer, M., Boike, J., et al. (2016). Simulating the thermal regime and thaw processes of ice-rich permafrost ground with the land-surface model CryoGrid 3. *Geoscientific Model Development*, *9*(2), 523-546. https://doi.org/10.5194/gmd-9-523-2016

Wu, Q., Hou, Y., Yun, H., et al. (2015). Changes in active-layer thickness and near-surface permafrost between 2002 and 2012 in alpine ecosystems, Qinghai–Xizang (Tibet) Plateau, China. *GLOBAL AND PLANETARY CHANGE*, *124*, 149-155. https://doi.org/10.1016/j.gloplacha.2014.09.002

Wu, X., & Nan, Z. (2016). *A multilayer soil texture dataset for permafrost modeling over Qinghai-Tibetan Plateau* 2016 IEEE International Geoscience and Remote Sensing Symposium (IGARSS), Beijing, China. https://doi.org/10.1109/igarss.2016.7730283

Wu, X., Nan, Z., Zhao, S., et al. (2018). Spatial modeling of permafrost distribution and properties on the Qinghai-Tibet Plateau. *Permafrost and Periglacial Processes*, *29*(2), 86-99. https://doi.org/10.1002/ppp.1971

Xiang, L., Wang, H., Steffen, H., et al. (2016). Groundwater storage changes in the Tibetan Plateau and adjacent areas revealed from GRACE satellite gravity data. *Earth and Planetary Science Letters*, *449*, 228-239. https://doi.org/10.1016/j.epsl.2016.06.002

Xu, F., Zhang, G., Woolway, R. I., et al. (2024). Widespread societal and ecological impacts from projected Tibetan Plateau lake expansion. *Nature Geoscience*. https://doi.org/10.1038/s41561-024-01446-w

You, Q., Chen, D., Wu, F., et al. (2020). Elevation dependent warming over the Tibetan Plateau: Patterns, mechanisms and perspectives. *Earth-Science Reviews*, *210*, 103349. https://doi.org/10.1016/j.earscirev.2020.103349

You, Q., Min, J., Zhang, W., et al. (2015). Comparison of multiple datasets with gridded precipitation observations over the Tibetan Plateau. *Climate Dynamics*, *45*(3), 806. https://dx.doi.org/10.1007/s00382-014-2310-6

Yuan, H., Ning, L., Zhou, J., et al. (2024). HiCPC: A new 10-km CMIP6 downscaled daily climate projections over China. *Scientific Data*, *11*(1), 1167. https://doi.org/10.1038/s41597-024-03982-x

Yuan, X., Yang, K., Lu, H., et al. (2021). Characterizing the features of precipitation for the Tibetan Plateau among four gridded datasets: Detection accuracy and spatio-temporal variabilities. *Atmospheric Research*, *264*, 105875. https://doi.org/10.1016/j.atmosres.2021.105875

Zhang, H., Immerzeel, W. W., Zhang, F., et al. (2022). Snow cover persistence reverses the altitudinal patterns of warming above and below 5000 m on the Tibetan Plateau. *Science of The Total Environment*, *803*, 149889. https://doi.org/10.1016/j.scitotenv.2021.149889

Zhang, H., Immerzeel, W. W., Zhang, F., et al. (2021). Creating 1-km long-term (1980–2014) daily average air temperatures over the Tibetan Plateau by integrating eight types of reanalysis and land data assimilation products downscaled with MODIS-estimated temperature lapse rates based on machine learning. *International Journal of Applied Earth Observation and Geoinformation*, *97*, 102295. https://doi.org/10.1016/j.jag.2021.102295

Zhang, Z., Wu, Q., Jiang, G., et al. (2020). Changes in the permafrost temperatures from 2003 to 2015 in the Qinghai-Tibet Plateau. *Cold Regions Science and Technology*, *169*, 102904. https://doi.org/10.1016/j.coldregions.2019.102904

Zhao, L., Zou, D., Hu, G., et al. (2021). A synthesis dataset of permafrost thermal state for the Qinghai–Tibet (Xizang) Plateau, China. *Earth System Science Data*, *13*(8), 4207-4218. https://doi.org/10.5194/essd-13-4207-2021

Zou, D., Pang, Q., Zhao, L., et al. (2024). Estimation of Permafrost Ground Ice to 10 m Depth on the Qinghai-Tibet Plateau. *Permafrost and Periglacial Processes*. https://doi.org/10.1002/ppp.2226

Zou, D. F., Zhao, L., Sheng, Y., et al. (2017). A new map of permafrost distribution on the Tibetan Plateau. *The Cryosphere*, *11*(6), 2527-2542. https://doi.org/10.5194/tc-11-2527-2017